Journal of Magnetism and Magnetic Materials 418 (2016) 54–61

Contents lists available at ScienceDirect

Journal of Magnetism and Magnetic Materials

journal homepage: www.elsevier.com/locate/jmmm

Effect of Gd–Ti co-substitution on structural, magnetic and electrical properties of multiferroic $BiFeO_3$

M. Gowrishankar, D. Rajan Babu *, S. Madeswaran

Advanced Materials Research Centre, School of Advanced Sciences, VIT University, Vellore 632014, India

ARTICLE INFO

Article history:
Received 7 January 2016
Received in revised form
18 March 2016
Accepted 29 March 2016
Available online 1 April 2016

Keywords:
$BiFeO_3$
Multiferroic
XPS
VSM
Arrott plot
Dielectric

ABSTRACT

$Bi_{1-x}Gd_xFe_{1-x}Ti_xO_3$ (x=0.05, 0.10, 0.15 and 0.20) powder was synthesized by a facile sol–gel route and the phase was confirmed by powder X-ray diffraction analysis. Rietveld analysis corroborates the following sequence of phase transitions with increasing concentration of x: rhombohedral ($R3c$) → orthorhombic (Pbnm) → cubic ($Pm\bar{3}m$). X-ray photoelectron spectroscopy revealed the fact that Fe exists predominantly as +3 state in the co-substituted sample. Scanning electron micrographs evidences the reduction in particle size with increase in concentration of the co-substituents. Broadening, suppression and shifting of Raman modes with the increase in concentration of Gd and Ti supports the structural phase transition. UV–Vis diffuse reflectance spectra showed a decrease in the energy gap with the increase of the co-substituent concentration. The magnetic behavior of the samples demonstrates the significant increase in latent magnetization with the increase in co-substituent concentration which was substantiated by Arrott–Belov–Kouvel plot. Temperature dependent dielectric analysis of the co-substituted samples showed an anomaly in the vicinity of Neel temperature (T_N) indicating a change in the magnetic ordering. The leakage current density is found to be decreased with the increase in concentration of Gd and Ti.

1. Introduction

Multiferroic materials offer a great deal of interest towards technical applications due to the coexistence of two or more ferroic orders such as ferroelectric, ferromagnetic, ferroelasticity and ferrotoroidicity in a single phase [1,2]. The most interesting feature of multiferroic system is the magnetoelectric (ME) coupling which leads the realization of mutual control of magnetism over electric polarization and vice versa. These materials have gained much importance in the field of spintronics and low field magnetic sensors due to the fundamental and fascinating aspects of physics [3]. Among those, $BiFeO_3$ (BFO) is a material which exhibits both ferromagnetic and ferroelectric behavior well above the room temperature [4].

The crystal structure of BFO is rhombohedral with a distorted perovskite structure which belongs to R3c space group at room temperature. Origin of ferroelectricity in BFO is ascribed to the presence of $6S^2$ lone pair of electrons in Bi^{3+}, whereas the magnetic property originates from the partially filled d orbital of Fe ion [5]. BFO possesses G-type antiferromagnetism with incommensurate spin cycloid of long repetitive range of 63 nm along [110] direction [6]. It has high ferroelectric ordering at T_C~870 °C and ferromagnetic ordering at T_N~370 °C. This wide range of ferroic transitions renders BFO a weakly coupled magneto-electric material which forbids its practical applications [7]. In addition to this, BFO is sternly influenced by the secondary phases such as $Bi_2Fe_4O_9$, $Bi_{25}FeO_{40}$ and $Bi_{36}Fe_{24}O_{57}$ as well as weak polarization, poor magnetization, hopping of Fe ions, low resistivity and high leakage current limit its usage in cutting edge applications [8].

We have adopted co-substitution strategy to overcome the drawbacks of BFO. Several reports have suggested that cationic substitution of rare earth element on A-site and transition element on B-site shows an effective reduction of leakage current density, enhancement of magnetization and improvement of ferroelectric behavior [9–12]. Recently, Yoo et al. reported the enhancement of ferromagnetic and ferroelectric polarization for the Dy and Co co-doped BFO [13]. Sati et al. confirmed the reduction of leakage current, improvement of ferromagnetic and dielectric behavior of Pr and Ti co-doped BFO [14]. Liu et al. suggested that (Sm, Mn, Cr) co-doping has effectively decreased the leakage current leading to the improvement of multiferroic properties [15].

Rare earth elements with relatively low electronegativity compared to oxygen have a strong influence on the ferroelectric and ferromagnetic property of BFO [11]. Doping the rare earth element Gd on Bi site reduces the particle size and increases its

* Corresponding author.
E-mail address: rajanbabuphy@gmail.com (D.R. Babu).

http://dx.doi.org/10.1016/j.jmmm.2016.03.085
0304-8853/

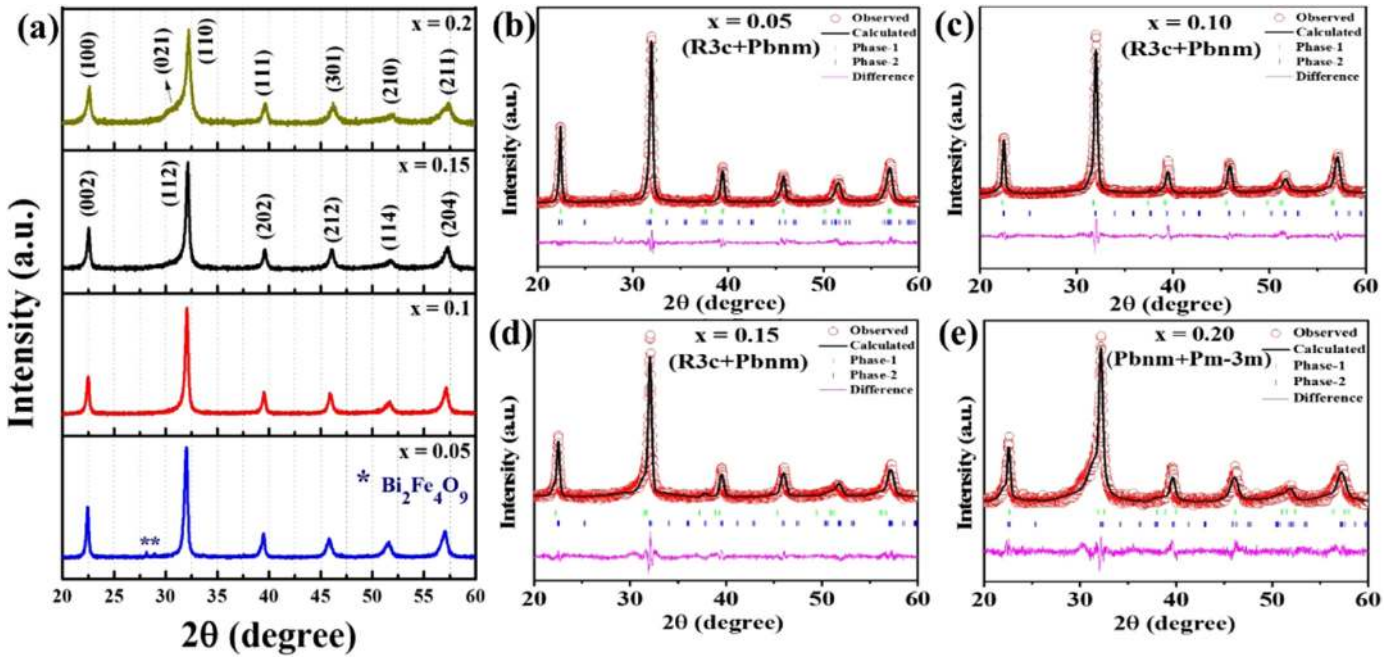

Fig. 1. (a) Powder XRD pattern and (b–e) Rietveld refinement patterns of $Bi_{1-x}Gd_xFe_{1-x}Ti_xO_3$ (x=0.05, 0.10, 0.15 and 0.20) nanoparticles.

Table 1
Parameters obtained from Rietveld refinement of XRD pattern for $Bi_{1-x}Gd_xFe_{1-x}Ti_xO_3$ (x=0.05, 0.10, 0.15 and 0.2).

x	Crystal structure	Lattice parameter (Å) Volume (Å^3)	Atomic positions				*R* factor (%)
0.05	Rhombohedral (R3c) 68.4%	a=5.612; c=13.703;V=373.738	Bi/Gd	0.0000	0.0000	−0.0362	wRp=8.89 Rp=6.97 χ^2=2.64
		Bond length (Å)					
		Bi/Gd–O 5.25153(9);	Fe/Ti	0.0000	0.0000	0.2245	
		Fe/Ti–O 8.6636(16)					
		Bond angle (deg)	O	0.4145	−0.0157	0.9387	
		O–Bi–O 120.12; O–Fe–O 106.74					
	Orthorhombic (Pbnm) 31.20%	a=5.626; b=5.68; c=7.894;V=252.287	Bi/Gd	0.0000	0.0318	0.2500	
		Bond length (Å)	Fe/Ti	0.0042	0.5000	0.0000	
		Bi/Gd–O 3.74(10); Fe/Ti–O 3.4977(9)					
		Bond angle (deg)	O1	0.4777	0.5650	0.2500	
		O–Bi–O 134; O–Fe–O 118.69	O2	−0.5115	0.4825	0.2262	
0.10	Rhombohedral (R3c) 46.95%	a=5.647; c=13.778;V=380.542	Bi/Gd	0.0000	0.00000	−0.0285	wRp=8.94 Rp=7.12 χ^2=2.43
		Bond length (Å)					
		Bi/Gd–O 4.306(17); Fe/Ti–O 1.2516(15)	Fe/Ti	0.00000	0.0000	0.2564	
		Bond angle (deg)	O	0.3082	−0.12823	0.9376	
		O–Bi–O 142.85; O–Fe–O 92.21					
	Orthorhombic (Pbnm) 53.05%	a=5.602; b=5.599; c=7.926; V=248.622	Bi/Gd	−0.0007	0.0021	0.2500	
		Bond length (Å)	Fe/Ti	0.0000	0.5000	0.0000	
		Bi/Gd–O 2.949(10); Fe/Ti–O 2.09(5)					
		Bond angle (deg)	O1	0.1127	0.4632	0.2500	
		O–Bi–O 99.69; O–Fe–O 67.89	O2	−0.3847	0.2487	0.0646	
0.15	Rhombohedral (R3c) 39.4%	a=5.681; c=13.767; V=384.854	Bi/Gd	0.0000	0.0000	−0.0401	wRp=9.2 Rp=7.38 χ^2=2.59
		Bond length (Å)					
		Bi/Gd–O 4.252(4); Fe/Ti–O 1.363(7)	Fe/Ti	0.0000	0.0000	0.2509	
		Bond angle (deg)					
		O–Bi–O 70.98; O–Fe–O 71.49	O	0.2273	−0.1648	0.9191	
	Orthorhombic (Pbnm) 60.6%	a=5.564; b=5.589; c=7.9;V=246	Bi/Gd	−0.0054	0.0041	0.2500	
		Bond length (Å)	Fe/Ti	0.0000	0.5000	0.0000	
		Bi/Gd–O 2.637(6); Fe/Ti–O 2.014(8)					
		Bond angle (deg)	O1	0.0674	0.4883	0.2500	
		O–Bi–O 67.09; O–Fe–O 80.04	O2	-0.2840	0.2919	0.0729	
0.20	Orthorhombic (Pbnm) 47.6%	a=6.035; b=6.1; c=9.349; V=340.365	Bi/Gd	−0.0070	−0. 0382	0.2500	wRp=8.73 Rp=6.94 χ^2=2.56
		Bond length (Å)	Fe/Ti	0.0000	0.5000	0.0000	
		Bi/Gd–O 4.692(7); Fe/Ti–O 1.73(3)					
		Bond angle (deg)	O1	0.0206	1.0681	0.2500	
		O–Bi–O 93.76; O–Fe–O 37.955	O2	−0.5015	1.1389	1.7615	
	Cubic ($pm\bar{3}m$) 52.4%	a=3.943; V=31.307	Bi/Gd	0.0000	0.0000	0.0000	
		Bond length (Å)					
		Bi/Gd–O 2.79(14); Fe/Ti–O 1.972(14)	Fe/Ti	0.50000	0.5000	0.5000	
		Bond angle (deg)					
		O–Bi–O 60; O–Fe–O 180	O	0.00000	0.50000	0.50000	

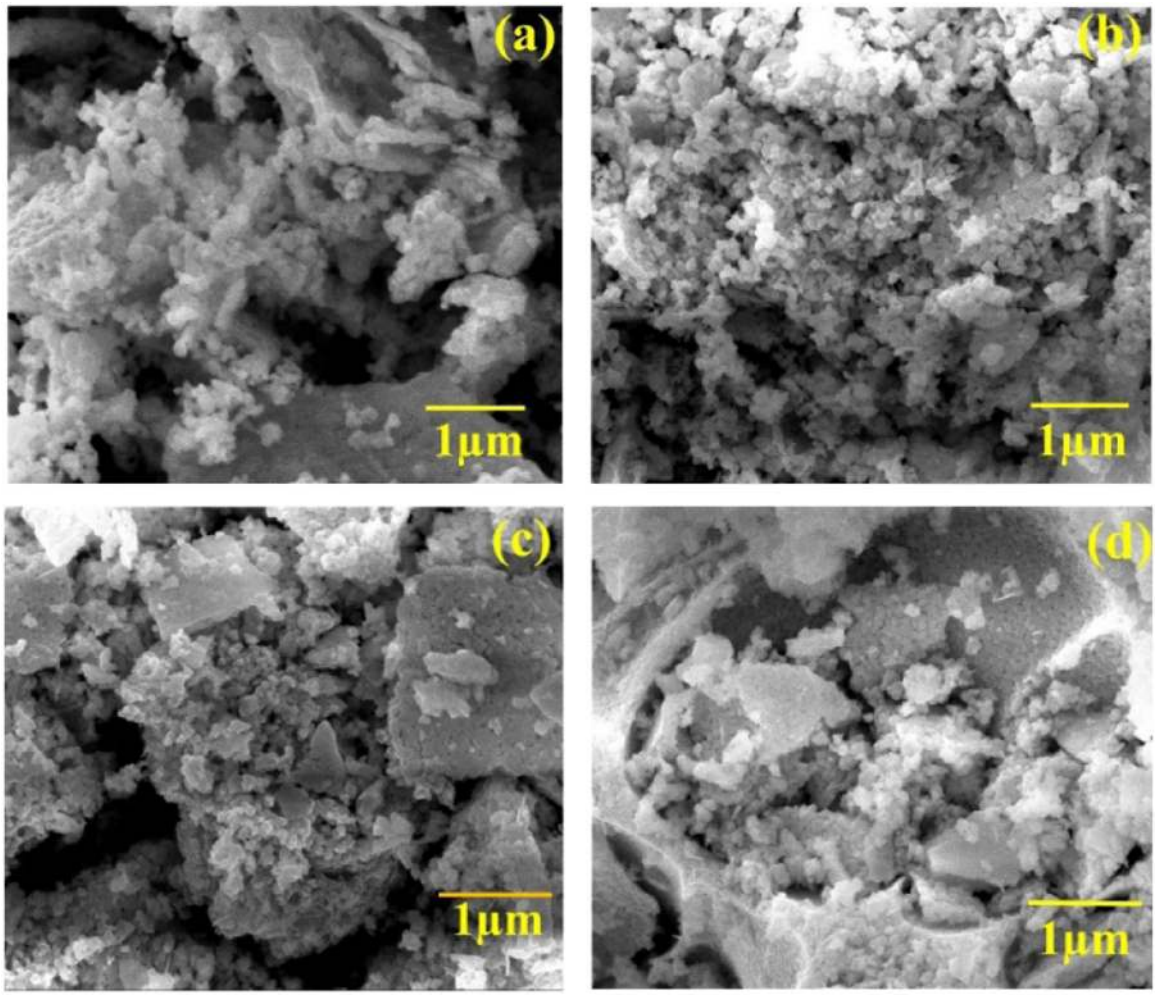

Fig. 2. (a–d) FE-SEM images for $Bi_{1-x}Gd_xFe_{1-x}Ti_xO_3$ ($x=0.05$, 0.10, 0.15 and 0.20) nanoparticles.

magnetic and electrical behavior [16–18]. Whereas, doping tetravalent Ti on Fe site compensates the charge, suppresses the secondary phases and optimizes Fe in +3 state. This in turn results in the suppression of oxygen deficiencies and decrease in leakage current density. It tends to increase the resistivity of BFO eventually ferroelectric behavior enhances [19–22]. Along these lines, we herein exploit the synthesis of Gd–Ti substituted BFO with the chemical formula $Bi_{1-x}Gd_xFe_{1-x}Ti_xO_3$ ($x=0.05$, 0.10, 0.15 and 0.20) powder using the sol–gel method and employed XPS to affirm the valence state of Fe. To the best of our knowledge, there are no reports available on the synthesis of Gd and Ti co-substituted $BiFeO_3$ by sol–gel method.

2. Experiment

$Bi_{1-x}Gd_xFe_{1-x}Ti_xO_3$ (for $x=0.05$, 0.1, 0.15 and 0.20) was synthesized by a sol–gel method. All the reagents were procured with ultra-high purity and used without further purification. For the current investigation, Bismuth nitrate pentahydrate [$Bi(NO_3)_3\cdot 5H_2O$] and Gadolinium acetate hydrate [$Gd(CH_3CO_2)_3\cdot H_2O$] were dissolved in dil.HNO_3 in a beaker. Similarly, Iron nitrate nonahydrate [$Fe(NO_3)_3\cdot 9H_2O$] and Titanium tetra isopropoxide [$Ti(OCH(CH_3)_2]_4$ were dissolved in deionized water in another beaker. Both the solutions were mixed under constant stirring. Tartaric acid was added to the homogeneous precursor solution as a chelating agent and the resultant solution was stirred constantly and heated to about 80 °C until the viscous gel was formed. The obtained gel was dried overnight, then preheated at 400 °C and ground thoroughly using mortar and pestle. The resultant powder was annealed at 600 °C at the rate of 10 °C/min for 4 h to acquire the fine crystalline product.

X-ray diffraction was carried out in Bruker D8 advance powder X-ray diffractometer using Cu-Kα (1.5406 Å) radiation. FEI Quanta FEG 200 FE-SEM was used to analyze the surface morphology of the samples. X-ray photoelectron spectroscopy (XPS) analysis was done in DAR400-XM1000 (OMICRON Nanotechnologies, Germany) instrument using dual Al/Mg anodes as X-ray source. Laser Raman spectra were recorded using the excitation source of wavelength 514 nm with a confocal scanning spectrometer (Renishaw in VIA). UV–vis absorption spectra were recorded using JASCO UV–Visible spectrometer (V-670 PC). FTIR spectra was studied using Shimadzu IR Affinity-1. The magnetic behavior of the samples at room temperature was analyzed using Lakeshore vibrating sample magnetometer (VSM). Temperature dependent dielectric analysis was carried out using PSM 1735 – NumetriQ, N4L impedance analyzer and leakage current density was measured using Agilent electrometer.

3. Results and discussion

The XRD patterns of $Bi_{1-x}Gd_xFe_{1-x}Ti_xO_3$ ($x=0.05$, 0.10, 0.15 and 0.20) are shown in Fig. 1(a). Lower intensity of secondary phase $Bi_2Fe_4O_9$ was observed at 28° and 28.8° for $x=0.05$ due to the

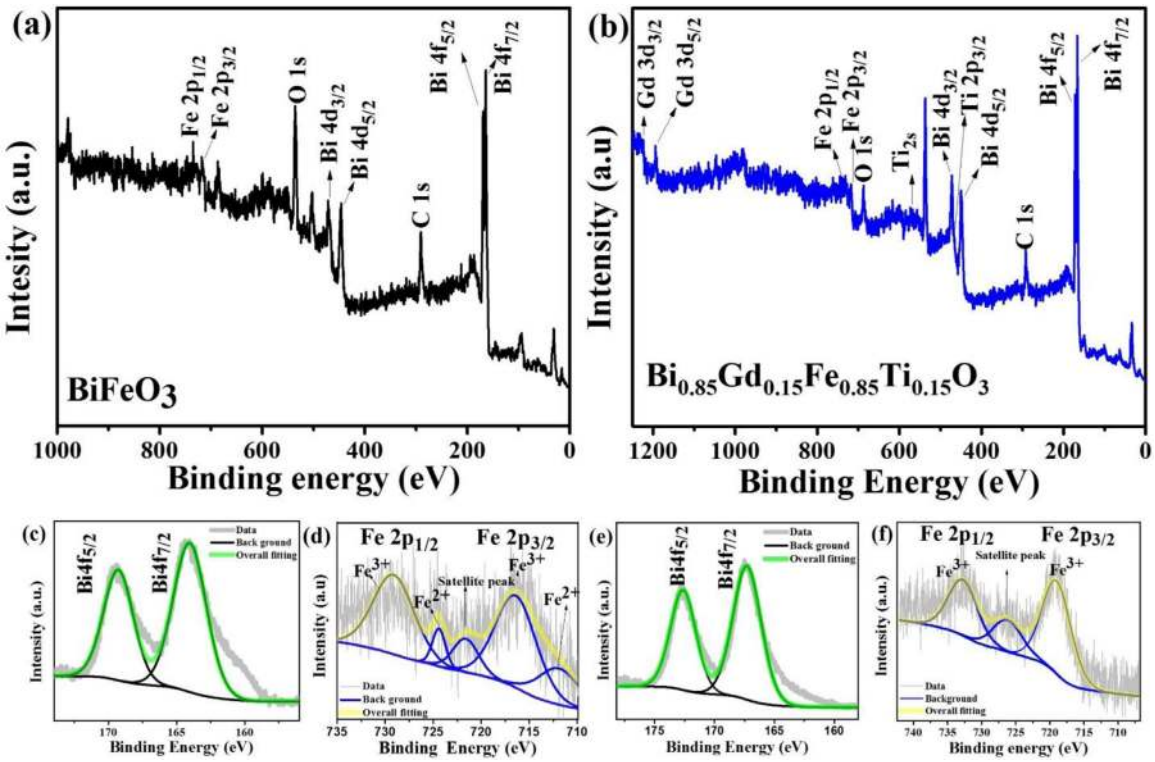

Fig. 3. (a and b) XPS Survey spectrum and (c-e) narrow window scan of Bi and Fe of Pure $BiFeO_3$ and $Bi_{0.85}Gd_{0.15}Fe_{0.85}Ti_{0.15}O_3$ respectively.

kinetics of phase formation. However, these secondary phases were suppressed for $x=0.10$, 0.15 and 0.20 which was ascribed to the increase in the concentration level of Gd and Ti. It is apparent from Fig. 1(a), that on increase in the concentration of the co-substituents, the XRD peaks tend to shift towards the higher angle of 2θ accompanied with the increase in broadening of peaks and suppression of prominent peaks. This signifies the inclusions of smaller ionic radii elements Gd (1.05 Å) on Bi (1.17 Å) and Ti (0.605 Å) on Fe (0.645 Å) sites respectively. The average crystallite size for each sample was calculated using the Scherrer's equation, $d = \frac{0.89\lambda}{\beta \cos\theta}$ (nm) where, λ is the wavelength of Cu - Kα, β is the full width at half maximum (FWHM) and θ is the Bragg angle. The calculated average crystallite size was found to be 21 nm, 22 nm, 21 nm and 14 nm for $x=0.05$, 0.10, 0.15 and 0.20, respectively.

The dopants induced degree of distortion was estimated using Goldschmidt tolerance factor (t), $t=\frac{(r_A+r_O)}{\sqrt{2}\,(r_B+r_O)}$ where r_A, r_B, and r_O are the ionic radii of A-site (Bi^{3+} and Gd^{3+}), B-site (Fe^{3+} and Ti^{4+}) and O^{2-} ions, respectively. The tolerance factor was found to be 0.8886, 0.886, 0.885 and 0.8838 for $x=0.05$, 0.10, 0.15 and 0.20 respectively, inferring that the lattice distortion increases with the increase in concentration of co-substituents [23,24]. The corresponding changes in the values of "t" were lesser than one which ensures the rotation of FeO_6 octahedron along [111] direction. It is well known that BFO crystallizes as rhombohedral with R3c space group [5]. As a result of this co-substitution, lattices were distorted in the host, weakened the rhombohedral (R3c) phase and induced the orthorhombic (Pbnm) phase formation for $x=0.05$. As the concentration was increased to 0.10 and 0.15, the amount of rhombohedral phase decreased considerably despite the gradual increase in orthorhombic phase. A further increase in the concentration to 0.20, resulted in the disappearance of the rhombohedral (R3c) phase which transformed to a new cubic ($pm\bar{3}m$) phase along with the existing orthorhombic (pbnm) phase. This is attributed to the chemical pressure of Gd and Ti induced lattice distortion of host BFO. The obtained results are in complete agreement with the reported literature of high pressure induced structural effects in BFO [25]. The transformed phases were confirmed by the Rietveld analysis of $Bi_{1-x}Gd_xFe_{1-x}Ti_xO_3$ compound using GSAS, as shown in Fig. 1(b–e) and the detailed refined parameters were tabulated in Table 1. The FE-SEM of all the co-substituted BFO samples are shown in Fig. 2(a–d). It indicates the agglomeration of particles, but it affirms the decrease in size with the increase in the concentration of the Gd and Ti. The decrease in the particle size can be attributed to the incorporation of Gd and Ti in $BiFeO_3$ system.

X-ray photoelectron spectroscopy (XPS) is an excellent technique to probe the chemical composition and charge state of the elements present in the compound. The survey spectrum confirms the presence of Bi, Fe, Gd, Ti and O in the prepared sample. The XPS survey spectrum recorded for Pure BFO and $Bi_{0.85}Gd_{0.15}Fe_{0.85}Ti_{0.15}O_3$ are shown in Fig. 3(a and b) and the corresponding core-level spectra of Bi and Fe are shown in Fig. 3(c – f). The XPS survey spectrum of pure BFO shows that Bi exists in +3 state and Fe in mixed valence state (+2 and +3). Binding energies of Bi $4f_{7/2}$, Bi $4f_{5/2}$, Fe $2p_{1/2}$ and Fe $2p_{3/2}$ peaks were observed at 167.5 eV, 173 eV, 719.3 eV and 732.92 eV respectively, for $Bi_{0.85}Gd_{0.15}Fe_{0.85}Ti_{0.15}O_3$. These results reveals that Bi exists in its favorable +3 state and Fe in predominant +3 valence state [24,26,27]. Thus, doping of Gd^{3+} in A-site and Ti^{4+} in B-site, restricts the hopping of Fe ions, which further leads to the suppression of oxygen vacancies and increase in the resistivity of BFO.

Raman spectra analysis were done to probe the structural and vibrational properties of the prepared samples, shown in Fig. 4(a). According to group theory, rhombohedral BFO has 18 optical phonon modes such as $4A_1$, $5A_2$ and 9E, where A_1 and A_2 are longitudinal optical (LO) modes and E is the transverse optical mode (TO). The $4A_1$ and 9E symmetric phonons are Raman active modes and remaining $5A_2$ modes are Raman inactive due to the absence of change in dipole moment. Therefore, totally thirteen Raman active modes are present in pure BFO. Raman spectroscopy is sensitive to the symmetry of crystalline structures and can

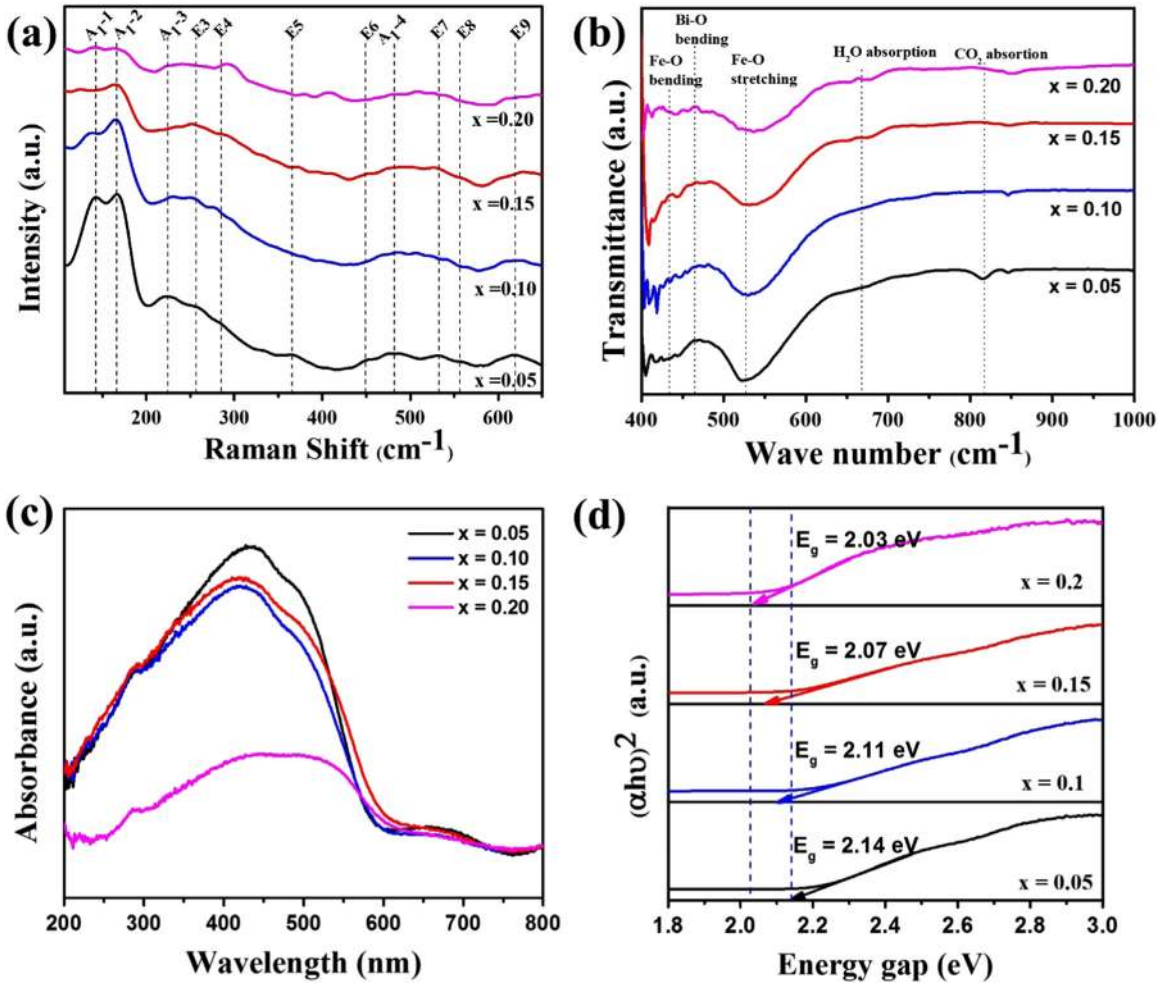

Fig. 4. (a) Raman spectra (b) FTIR spectra (c) UV–Vis absorption spectra and (d) Tauc plot of $Bi_{1-x}Gd_xFe_{1-x}Ti_xO_3$ (x=0.05, 0.10, 0.15 and 0.20) nanoparticles.

Table 2
Raman modes of $Bi_{1-x}Gd_xFe_{1-x}Ti_xO_3$ (x=0.05, 0.10, 0.15 and 0.2).

Raman mode (cm^{-1})	x=0.05	x=0.10	x=0.15	x=0.20
A_1-1	141	137	125	141
A_1-2	166	165	166	172
A_1-3	224	223	235	240
A_1-4	482	483	502	510
E3	256	256	256	-
E4	283	277	290	294
E5	367	380	374	382
E6	449	466	448	406
E7	532	544	532	478
E8	557	567	560	544
E9	619	615	626	611

therefore be used to study the structural phase transition of BFO with the increase in concentration of Gd and Ti. According to group theory, A_1 phonon modes in the lower frequency region ($<400\ cm^{-1}$) are ascribed to the Bi–O vibration and E phonon modes in higher frequencies are responsible for Fe–O vibrations [11]. As shown in the Fig. 4(a), there are eleven Raman modes for x=0.05 which includes four A_1 modes and seven E modes. When compared with pure BFO, shifting of the Raman modes were found for x=0.05 which can be attributed to the lattice distortion induced by Gd and Ti on host BFO [28]. The observed Raman modes demonstrates the fact that there is peak shifting as well as broadening accompanied with variation in intensity of peaks for the increase in concentration of x (0.10–0.2). This change in structural transitions has been substantiated by the Rietveld refinement. The obtained peak position of the Raman modes for $Bi_{1-x}Gd_xFe_{1-x}Ti_xO_3$ (x=0.05, 0.10, 0.15 and 0.20) are listed in Table 2.

The room temperature FTIR spectra recorded for $Bi_{1-x}Gd_xFe_{1-x}Ti_xO_3$ (for x=0.05, 0.10, 0.15 and 0.20) in the wave number range of 400–1000 cm^{-1} are shown in Fig. 4(b). The wave number range 400–675 cm^{-1} shows the typical band characteristics of metal oxygen bonds. Two strong absorption peaks were observed near 435 cm^{-1} and 525 cm^{-1} assigned to the Fe–O bending and stretching vibrations respectively. The presence of a broad band around 470 cm^{-1} is due to the existence of BiO_6 octahedra along with FeO_6 complex group. Further, the FTIR spectra reveal the softening of vibration modes on increase in the concentration of Gd and Ti, which is due to the concomitant structural phase transitions as confirmed by the XRD analysis.

The UV–vis absorption spectra and the corresponding Tauc's plot for the prepared samples are shown Fig. 4(c and d). The strong band observed in the wavelength range of 450–600 nm is attributed to metal–metal transition and the weak band around 700 nm is assigned to the crystal field transitions. The absorption cut-off wavelength increases with the increase in concentration of the co-substituents and the corresponding energy gap (E_g) values were calculated from Wood and Tauc relation: $\alpha h\upsilon = (h\upsilon - E_g)^n$ where, α is the absorption coefficient, h in the Planck's constant, υ is the frequency, E_g is the optical energy gap and n is the number associated with the different types of electronic transitions and it is ½ for direct band gap.

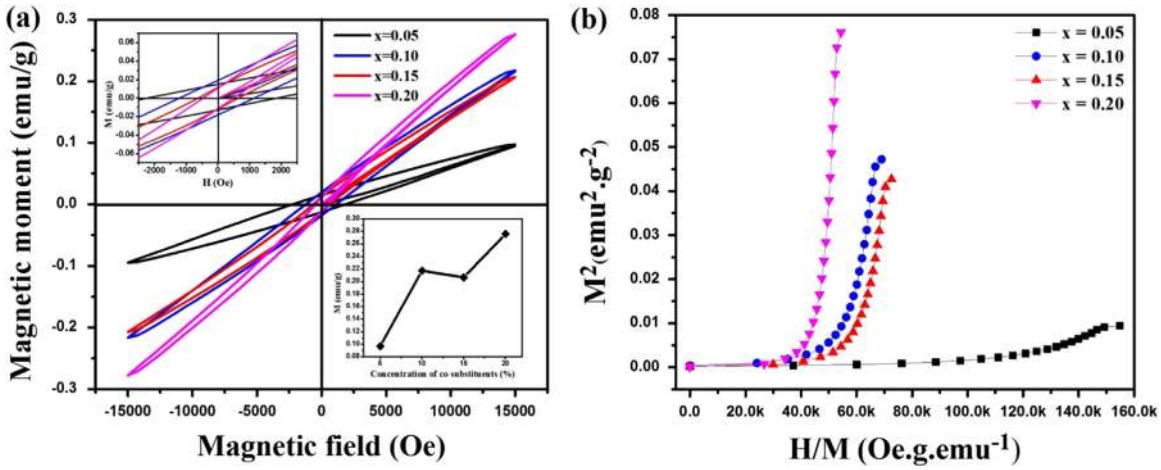

Fig. 5. (a) M-H loop and (b) Arrott–Belov–Kouvel (ABK) plot for $Bi_{1-x}Gd_xFe_{1-x}Ti_xO_3$ (x=0.05, 0.10, 0.15 and 0.20). Insets of 5(a) Enlarged scale between −2.5 kOe and +2.5 kOe and Magnetization values at higher field of 15 kOe.

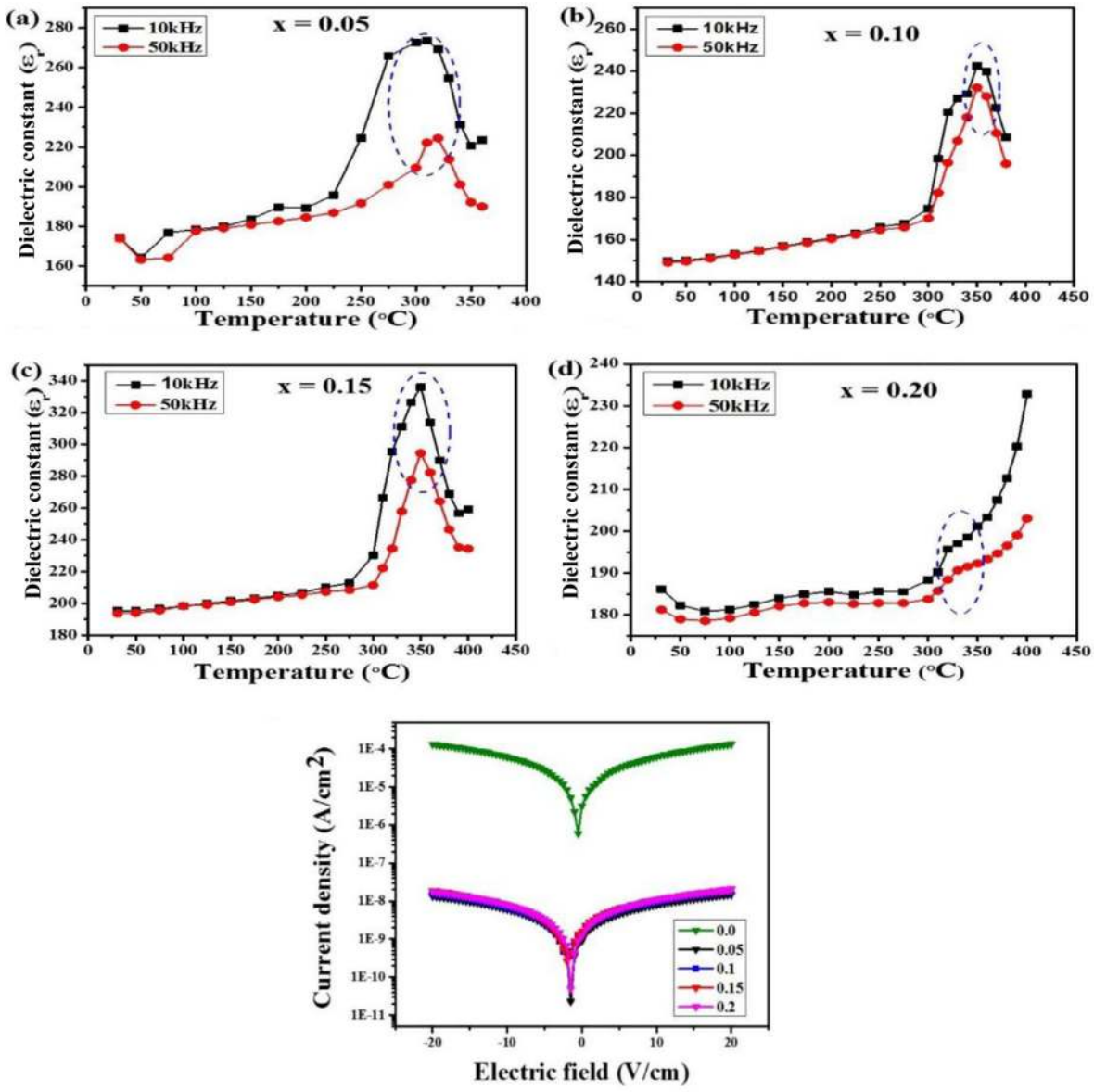

Fig. 6. (a) Temperature dependent dielectric analysis and (b) leakage current measurement for $Bi_{1-x}Gd_xFe_{1-x}Ti_xO_3$ (x=0.05, 0.10, 0.15 and 0.20) nanoparticles.

The measured energy band gap was found to be 2.14 eV, 2.11 eV, 2.07 eV and 2.03 eV for the co-substituted samples. The band gap values of co-substituted BFO are smaller than that of pure BFO which was reported as ~2.8 eV [29]. The observed changes in E_g may be due to the size effect and the structural distortion induced in the host. In particular, co-substitution of Gd and Ti in BFO induces change of Fe–O–Fe bond angles due to the ocatahedral distortion. The obtained narrow optical energy band gap value suggests that Gd and Ti co-substituted BFO samples would be a potential candidate towards the application of visible-light photocatalyst [30].

The magnetic properties of $Bi_{1-x}Gd_xFe_{1-x}Ti_xO_3$ ($x=0.05$, 0.1, 0.15 and 0.20) nanoparticles were studied at room temperature and the respective M-H loops are shown in the Fig. 5(a). The corresponding magnetic parameters are depicted in the insets of Fig. 5(a). Despite BFO being antiferromagnetic with a spiral spin cycloidal structure, there was an enhancement in the latent magnetization of the samples with the increase in the concentration of Gd and Ti. Arrott–Belov–Kouvel (ABK) plot (H/M vs M^2) shown in Fig. 5(b) is used to demonstrate the increase in magnetic behavior of the samples. It reveals that as the concentration increases from $x=0.05$ to 0.20, the concave nature of the plotted curves (H/M vs M^2) slowly tend to decrease with the increase in the concentration of x confirms the increase in ferromagnetic nature of the co-substituted samples [31].

The reason for increase in magnetization of Gd and Ti co-substituted BFO can be accounted as follows: (i) reduced particle size, (ii) co-substitution induced Jahn–Teller distortion, (iii) increase in magnetic interaction between Bi and Fe sites and (iv) alignment of canted spin structure and release of net magnetic moment [27]. Thus doping Gd on A-site and doping Ti on B-site of BFO impart the changes in the bond length of Fe–O – Fe and tilting of FeO_6 octahedra results in the cancellation of the long range spin cycloid and increases the latent magnetization [32].

The magnetization values at maximum field of 15 kOe were found to be 0.096 emu/g, 0.217 emu/g, 0.207 emu/g and 0.276 emu/g for $Bi_{1-x}Gd_xFe_{1-x}Ti_xO_3$ ($x=0.05$, 0.1, 0.15 and 0.20). The increasing trend in magnetic behavior for x=0.05 and 0.10 could be attributed to the co-substitution induced transition from the spatially modulated spiral spin structure to a homogenously weak ferromagnetic behavior. A typical decrease in both the remnant magnetization and the coercive field was observed for $x=0.15$, which evinces that the magnetic moment of Gd ($m=8.0\ \mu_B$) and nonmagnetic Ti tends to align antiparallel with respect to a weak ferromagnetic component associated with the Fe sublattice. In contrast, there is an increase in the magnetic behavior for $x=0.20$ which is associated with the subsequent phase transition to the cubic ($Pm\bar{3}m$) phase along with the existing orthorhombic (Pbnm) structure [33,34]. Moreover it was observed that coercivity of all the samples tends to decrease with increase in concentration of the co-substituents. This can be attributed to the decrease in magneto crystalline anisotropy [35].

Fig. 6(a) shows the temperature dependent dielectric response of Gd and Ti co-substituted BFO samples at 10 kHz and 50 kHz. It is observed that the dielectric constant of the samples exhibit lower values at lower frequencies and higher values at higher frequencies which are ascribed to the Maxwell–Wagner type of interfacial polarization, in concordance with Koop's phenomenological hypothesis [4]. The dielectric anomaly was observed in all the samples at 310 °C for $x=0.05$, 350 °C for $x=0.10$ and 0.15 and 330 °C for $x=0.20$. These dielectric anomaly occurs due to the change in the magnetic ordering from antiferromagnetic to paramagnetic transition which is accounted as Neel temperature (T_N). This kind of anomaly usually occurs in the magneto electric ordered systems which was demonstrated by the Landau–Devonshire theory of phase transitions [36]. It is observed that the increase in T_N from 310 °C to 350 °C for $x=0.05$ to $x=0.10$, 0.15 can be attributed to the structural phase transition from rhombohedral (R3c) to orthorhombic (Pbnm) system. Nevertheless, T_N decreases to 330 °C for $x=0.20$ can be ascribed to the co-substitution induced structural phase transition to cubic ($Pm\bar{3}m$) structure. The obtained anomalies for the co-substituted BFO were reported by many other research groups which corroborates the outcome of magnetoelectric effect [24,37,38].

The leakage current of the prepared samples were measured at room temperature by applying varying electric field as shown in Fig. 6(d). The fact behind high leakage current in BFO can be attributed to the presence of oxygen vacancies and hopping of Fe between +2 and +3 charge state. The oxygen vacancies are the trapping centers for the electrons and once the field is applied they are readily activated for conduction [39]. The leakage current for $Bi_{1-x}Gd_xFe_{1-x}Ti_xO_3$ ($x=0.05$, 0.1, 0.15 and 0.20) was found to be reduced by 3–4 orders as compared to pure BFO [40]. This can be attributed to the suppression of oxygen vacancies induced mainly due to the volatilization of Bi ion in the lattice. The electronic conduction in BFO is also related to the hopping of Fe^{2+} and Fe^{3+} ions. Therefore, substituting rare earth element on A-site and tetravalent Ti on B-site effectively inhibits the oxygen vacancies and suppresses the leakage current density.

4. Conclusion

$Bi_{1-x}Gd_xFe_{1-x}Ti_xO_3$ (for $x=0.05$, 0.10, 0.15 and 0.20) was synthesized using sol–gel method. Rietveld refinement of the XRD pattern confirmed the phase transition from rhombohedral (R3c) to orthorhombic (Pbnm) and then to cubic ($Pm\bar{3}m$) with the increase in the concentration of the co-substituents. XPS analysis revealed the existence of Fe in a single oxidation state (+3) leading to the suppression of oxygen vacancies. Band gap energy of the samples was calculated using Tauc's plot from the UV–vis diffuse reflectance spectra and the values were found to be 2.14, 2.1, 2.07 and 2.03 eV. M–H loop showed an increase in the latent magnetization due to the cancellation of the spiral spin cycloid. Dielectric anomaly was observed at 310 °C for $x=0.05$, 350 °C for $x=0.10$ and 0.15 and 330 °C for $x=0.20$ in the vicinity of Neel temperature (T_N). Leakage current density of the co-substituted samples was reduced by 3–4 orders as compared to the bulk BFO. Hence, co-substituting rare earth element Gd on Bi – site and tetravalent transition element Ti on Fe – site was found to be a very effective strategy in enhancing ferromagnetic and electric behavior simultaneously.

Acknowledgments

The authors are thankful to the management of VIT University, Vellore, India for providing financial support and encouragement through VIT-RGEMS Project (34/02.01.2014/VIT-RGEMS). One of the authors, MG acknowledges the Research Associateship offered by VIT University.

References

[1] J.-P. Rivera, A short review of the magnetoelectric effect and related experimental techniques on single phase (multi-) ferroics, Eur. Phys. J. B 71 (2009) 299–313.
[2] L.W. Martin, D.G. Schlom, Advanced synthesis techniques and routes to new single-phase multiferroics, Curr. Opin. Solid State Mater. Sci. 16 (2012) 199–215.
[3] Y. Wang, J. Hu, Y. Lin, C.-W. Nan, Multiferroic magnetoelectric composite

nanostructures, NPG Asia Mater. 2 (2010) 61–68.
[4] G. Catalan, J.F. Scott, Physics and applications of bismuth ferrite, Adv. Mater. 21 (2009) 2463–2485.
[5] L. Zhang, Y. Yang, S. Ma, W. Luo, Y. Liu, K. Zhu, Effect of magnetic annealing on phonon behaviors of nanocrystalline $BiFeO_3$, Phys. B Condens. Matter 407 (2012) 494–499.
[6] J.-G. Park, M.D. Le, J. Jeong, S. Lee, Structure and spin dynamics of multiferroric $BiFeO_3$, J. Phys. Condens. Matter 26 (2014) 433202.
[7] J. Xu, G. Ye, M. Zeng, Structure transition and enhanced multiferroic properties of Dy-doped $BiFeO_3$, J. Alloy. Compd. 587 (2014) 308–312.
[8] D. Hong, S. Yu, J. Cheng, Sm–Ti co-substituted $BiFeO_3$ thin films prepared by sol–gel technique, Curr. Appl. Phys. 11 (2011) S255–S259.
[9] X. Li, X. Wang, Y. Li, W. Mao, P. Li, T. Yang, et al., Structural, morphological and multiferroic properties of Pr and Co co-substituted $BiFeO_3$ nanoparticles, Mater. Lett. 90 (2013) 152–155.
[10] X. Yan, G. Tan, W. Liu, H. Ren, A. Xia, Structural, electric and magnetic properties of Dy and Mn co-doped $BiFeO_3$ thin fi lms, Ceram. Int. 41 (2015) 3202–3207.
[11] C.M. Raghavan, J.W. Kim, S.S. Kim, Effects of (Dy, Zn) co-doping on structural and electrical properties of $BiFeO_3$ thin films, Ceram. Int. 40 (2014) 2281–2286.
[12] Q. Yun, W. Xing, J. Chen, W. Gao, Y. Bai, S. Zhao, Effect of Ho and Mn co-doping on structural, ferroelectric and ferromagnetic properties of $BiFeO_3$ thin films, Thin Solid Films 584 (2015) 103–107.
[13] Y.J. Yoo, J.S. Hwang, Y.P. Lee, J.S. Park, J.Y. Rhee, J. Kang, et al., Origin of enhanced multiferroic properties in Dy and Co co-doped $BiFeO_3$ ceramics, J. Magn. Magn. Mater. 374 (2014) 669–675.
[14] P.C. Sati, M. Kumar, S. Chhoker, Raman spectroscopy and enhanced magnetic and dielectric properties of Pr and Ti codoped $BiFeO_3$ ceramics, J. Mater. Sci.: Mater. Electron. 26 (2015) 530–538.
[15] W. Liu, G. Tan, X. Xue, G. Dong, H. Ren, A. Xia, Phase transition and enhanced multiferroic properties of (Sm, Mn and Cr) co-doped $BiFeO_3$ thin films, Ceram. Int. 40 (2014) 12179–12185.
[16] G.S. Lotey, N.K. Verma, Structural, magnetic, and electrical properties of Gd-doped $BiFeO_3$ nanoparticles with reduced particle size, J. Nanopart. Res. 14 (2012) 742.
[17] S.K. Pradhan, J. Das, P.P. Rout, S.K. Das, D.K. Mishra, D.R. Sahu, et al., Defect driven multiferroicity in Gd doped $BiFeO_3$ at room temperature, J. Magn. Magn. Mater. 322 (2010) 3614–3622.
[18] A. Mukherjee, S. Basu, P.K. Manna, S.M. Yusuf, M. Pal, Enhancement of multiferroic properties of nanocrystalline $BiFeO_3$ powder by Gd-doping, J. Alloy. Compd. 598 (2014) 142–150.
[19] M. Kumar, K.L. Yadav, Study of room temperature magnetoelectric coupling in Ti substituted bismuth ferrite system, J. Appl. Phys. 100 (2006) 23–26.
[20] M.S. Bernardo, T. Jardiel, M. Peiteado, F.J. Mompean, M. Garcia-Hernandez, M. A. Garcia, et al., Intrinsic compositional inhomogeneities in bulk Ti-doped $BiFeO_3$: microstructure development and multiferroic properties, Chem. Mater. 25 (2013) 1533–1541.
[21] W. Cai, C. Fu, R. Gao, W. Jiang, X. Deng, G. Chen, Photovoltaic enhancement based on improvement of ferroelectric property and band gap in Ti-doped bismuth ferrite thin films, J. Alloy. Compd. 617 (2014) 240–246.
[22] L. Hongri, L. Zuli, L. Xiaolu, Y. Kailun, Effects of substitution of Ti for Fe in $BiFeO_3$ films prepared by sol–gel process, Phys. B Condens. Matter 400 (2007) 252–256.
[23] G. Rojas-George, J. Silva, R. Castañeda, D. Lardizábal, O. Graeve, L. Fuentes, et al., Modifications in the rhombohedral degree of distortion and magnetic properties of Ba- doped $BiFeO_3$ as a function of synthesis methodology, Mater. Chem. Phys. 146 (2014) 73–81.
[24] M. Gowrishankar, D. Rajan Babu, P. Saravanan, Room temperature multiferroism in La and Ti co-substituted $BiFeO_3$ nanoparticles, Mater. lett. 171 (2016) 34–37.
[25] R. Haumont, P. Bouvier, A. Pashkin, K. Rabia, S. Frank, B. Dkhil, W.A. Crichton, C.A. Kuntscher, J. Kreisel, Effect of high pressure on multiferroic $BiFeO_3$, Phys. Rev. B 79 (2009) 184110.
[26] S. Farhadi, N. Rashidi, Preparation and characterization of pure single-phase $BiFeO_3$ nanoparticles through thermal decomposition of the heteronuclear $Bi[Fe(CN)_6]\cdot 5H_2O$ complex, Polyhedron 29 (2010) 2959–2965.
[27] K. Saravana Kumar, P. Aswini, C. Venkateswaran, Effect of Tb–Mn substitution on the magnetic and electrical properties of $BiFeO_3$ ceramics, J. Magn. Magn. Mater. 364 (2014) 60–67.
[28] D. Kothari, V. Raghavendra Reddy, V.G. Sathe, A. Gupta, A. Banerjee, A. M. Awasthi, Raman scattering study of polycrystalline magnetoelectric $BiFeO_3$, J. Magn. Magn. Mater. 320 (2008) 548–552.
[29] A. Kumar, R.C. Rai, N.J. Podraza, S. Denev, M. Ramirez, Y. Chu, et al., Linear and nonlinear optical properties of $BiFeO_3$, Appl. Phys. Lett. 92 (121915) (2008) 29–31.
[30] A. Azam, A. Jawad, A.S. Ahmed, M. Chaman, a H. Naqvi, Structural, optical and transport properties of Al^{3+} doped $BiFeO_3$ nanopowder synthesized by solution combustion method, J. Alloy. Compd. 509 (2011) 2909–2913.
[31] J. Ray, A.K. Biswal, S. Acharya, V. Ganesan, D.K. Pradhan, P.N. Vishwakarma, Effect of Co substitution on the magnetic properties of $BiFeO_3$, J. Magn. Magn. Mater. 324 (2012) 4084–4089.
[32] V.B. Naik, R. Mahendiran, Magnetic and magnetoelectric studies in pure and cation doped $BiFeO_3$, Solid State Commun. 149 (2009) 754–758.
[33] V.A. Khomchenko, J.A. Paixão, V.V. Shvartsman, P. Borisov, W. Kleemann, D. V. Karpinsky, A.L. Kholkin, Effect of Sm substitution on ferroelectric and magnetic properties of $BiFeO_3$, Scr. Mater. 62 (2010) 238–241.
[34] M.A. Basith, O. Kurni, M.S. Alam, B.L. Sinha, B. Ahmmad, Room temperature dielectric and magnetic properties of Gd and Ti co-doped $BiFeO_3$ ceramics, J. Appl. Phys. 115 (2014) 024102.
[35] P. Sharma, V. Verma, Structural, magnetic and electrical properties of La and Mn co-substituted BFO samples prepared by the sol–gel technique, J. Magn. Magn. Mater. 374 (2015) 18–21.
[36] P. Uniyal, K.L. Yadav, Study of dielectric, magnetic and ferroelectric properties in $Bi_{1-x}Gd_xFeO_3$, Mater. Lett. 62 (2008) 2858–2861.
[37] D.-C. Jia, J.-H. Xu, H. Ke, W. Wang, Y. Zhou, Structure and multiferroic properties of $BiFeO_3$ powders, J. Eur. Ceram. Soc. 29 (2009) 3099–3103.
[38] M. Muneeswaran, N.V. Giridharan, Effect of Dy-substitution on the structural, vibrational, and multiferroic properties of $BiFeO_3$ nanoparticles, J. Appl. Phys. 115 (2014) 214109.
[39] H. Ishiwara, Impurity substitution effects in $BiFeO_3$ thin films – from a viewpoint of FeRAM applications, Curr. Appl. Phys. 12 (2012) 603–611.
[40] L.H. Yin, B.C. Zhao, J. Fang, R.R. Zhang, X.W. Tang, W.H. Song, et al., Improved leakage current and ferromagnetic properties in magnetic field annealed $BiFeO_3$-based ceramics, J. Solid State Chem. 194 (2012) 194–198.